Journal of Energy Chemistry 111 (2025) 86–93

Contents lists available at ScienceDirect

Journal of Energy Chemistry

journal homepage: www.elsevier.com/locate/jechem

http://www.journals.elsevier.com/journal-of-energy-chemistry/

# Mitigating lithium void formation in all-solid-state batteries via a high lithium diffusion 3D composite interlayer ☆

Zi-Ning Cheng [a,1], Xue-Yan Huang [b,1], Chen-Zi Zhao [b,*], Fang Fu [b], Jun-Dong Zhang [b], Jiang-Kui Hu [c], Yuqiong Mao [d], Languang Lu [d], Chun-Li Guo [a,*], Qiang Zhang [b,e,f]

[a] College of Materials Science and Engineering, Taiyuan University of Technology, Taiyuan 030024, Shanxi, China
[b] Beijing Key Laboratory of Complex Solid State Batteries & Tsinghua Center for Green Chemical Engineering Electrification, Department of Chemical Engineering, Tsinghua University, Beijing 100084, China
[c] The Innovation Center for Smart Solid State Batteries, Yibin 644002, Sichuan, China
[d] State Key Laboratory of Intelligent Green Vehicle and Mobility, School of Vehicle and Mobility, Tsinghua University, Beijing 100084, China
[e] State Key Laboratory of Chemical Engineering and Low-Carbon Technology, Tsinghua University, Beijing 100084, China
[f] Institute for Carbon Neutrality, Tsinghua University, Beijing 100084, China

ARTICLE INFO

*Article history:*
Received 25 May 2025
Revised 6 July 2025
Accepted 10 July 2025
Available online 23 July 2025

*Keywords:*
All solid-state lithium metal batteries
Interlayer
Solid-solid contacts
Lithium voids
Diffusion rates

ABSTRACT

With the ever-increasing energy density requirements for sulfide-based all-solid-state batteries, lithium metal is regarded as an ideal candidate for anode materials. However, the dynamic degradation of solid-solid contact between lithium anode and solid electrolyte remains a major challenge for the application of all-solid-state lithium metal batteries (ASSLMBs). The poor solid-solid contact problem is caused by the continuous accumulation of lithium voids, which results from the limited diffusion rate of lithium in the bulk phase. In this study, we design a three-dimensional (3D) lithiophilic graphitized carbon nanotube-based (LNT) interlayer to address interfacial issues. The interlayers effectively regulate lithium stripping and suppress the growth of lithium voids via improved lithium diffusion, leading to a conformal interface during continuous cycling. The lithium metal anode with the interlayer delivers an areal capacity of 12.96 mA h $cm^{-2}$, and when paired with a $LiNi_{0.9}Co_{0.05}Mn_{0.05}O_2$ (NCM9) cathode, the battery retains over 91% capacity retention after 100 cycles at room temperature. This work provides an effective strategy for interface stabilization in high-capacity and long-life ASSLMBs.



## 1. Introduction

With the growing demand for high-energy-density storage in electric vehicles and portable electronic devices, all-solid-state batteries (ASSBs) have attracted significant attention due to their enhanced safety and potential for higher energy density [1–5]. Among various anode materials, lithium metal (Li) stands out as a research focus for all-solid-state battery anodes due to its exceptionally high theoretical specific capacity (3860 mA h $g^{-1}$) and extremely low electrochemical potential (–3.04 V vs. standard hydrogen electrode) [6–10]. However, Li anodes still face numerous challenges in practical applications, among which the interfacial contact issues between the anode and solid-state electrolyte (SSE) are particularly prominent, significantly limiting the performance and cycle life of ASSBs [11–17]. The interface between solid-state electrolytes and lithium metal involves solid-solid contact, where achieving perfect surface conformity is inherently challenging due to limited point-to-point contact [18–21]. During electrochemical cycling, repeated volumetric expansion and contraction of lithium metal induce interfacial stress concentration, which compromises interface stability. This process leads to progressive void accumulation and pore formation, ultimately exacerbating interfacial contact issues [22–28].

The establishment of a stable electrochemical interface is critical for the practical application of ASSBs [29–32]. At non-ideal Li/SSE interfaces with existing defects, vacancies diffuse more rapidly along defective surfaces than into the bulk lithium metal.

☆ This article is part of a special issue entitled: 'Nova of Energy Chemistry' published in Journal of Energy Chemistry.

* Corresponding authors.
*E-mail addresses:* zcz@mail.tsinghua.edu.cn (C.-Z. Zhao), guochunli@tyut.edu.cn (C.-L. Guo).

[1] These authors contributed equally to this work.

https://doi.org/10.1016/j.jechem.2025.07.033

Consequently, vacancies become trapped/absorbed by defects, promoting defect growth [33–38]. Techniques such as applying external pressure, melting lithium metal, or constructing artificial interlayers can be employed to improve anode-electrolyte interfacial contact [39–43].

The introduction of interlayer between Li and the SSE is currently the most widely adopted approach to address the aforementioned issues [44–46]. In previously reported studies, this strategy has been shown to significantly improve interfacial contact and enhance stability. However, it cannot fundamentally resolve the problems of dendrite penetration and void formation during Li deposition and dissolution at the interface [47–49]. Common interlayer materials include polymers, alloys, and carbon-based materials. While polymer interlayers exhibit excellent mechanical stability, they often induce undesirable side reactions [50]. Lithium alloy interlayers demonstrate advantageous characteristics including lithiophilicity and high lithium-ion diffusivity, yet their fabrication involves complex processes with stringent technical requirements [51,52]. Carbon interlayers have been extensively studied, though their inherently low lithium diffusivity typically necessitates incorporation with fast ion-conducting materials [53–56]. In all-solid-state lithium metal batteries (ASSLMBs), lithium deposition generates substantial interfacial stress, potentially causing electrolyte cracking and lithium penetration at the Li/SSE interface. Conversely, lithium stripping leads to void formation and increased impedance due to limited bulk diffusion in lithium metal. Both deposition and stripping processes are confined to the interfacial region, where high current densities promote stress concentration and vacancy accumulation. These phenomena ultimately result in dendritic growth, interlayer degradation, void formation, and current focusing at the interface [57–61].

These issues can be addressed by applying external pressure or elevating temperature, which enhances lithium metal diffusion rates and consequently alleviates stress accumulation and vacancy aggregation at the Li/SSE interface [35,62–65]. However, precise temperature and pressure control would introduce additional costs and technical challenges for the practical implementation of ASSLMBs. The aforementioned results demonstrate that improving lithium-ion transport efficiency can effectively suppress dendritic growth and void formation at the interface [57,66,67]. In this regard, constructing three-dimensional (3D) lithiophilic interlayers to accelerate lithium transport within the anode represents a promising approach [68–70].

This contribution proposes an effective strategy to suppress Li voids by constructing a 3D lithiophilic graphitized carbon nanotube-based interlayer on the lithium anode, thereby stabilizing the dynamic interfacial contact between the anode and SSE during cycling. Homogeneous $LiC_6$ is formed in the interlayer through in situ Li intercalation into the carbon framework. The $LiC_6$ demonstrates lithiophilic characteristics, effectively guiding $Li^+$ deposition and enhancing stability during repeated Li plating/stripping cycles. The 3D framework constructed by lithiophilic graphitized carbon nanotube and fluorinated graphite effectively maintains interfacial contact between the Li anode and SSE, enabling Li nucleation at the interlayer interface followed by reversible infiltration/extraction during plating/stripping cycles. The synergistic construction of Li diffusion pathways with enhanced transport kinetics enables rapid annihilation of Li voids generated at the anode interface during stripping, thereby fundamentally mitigating dynamic contact instability caused by vacancy accumulation. The results demonstrate that full cells assembled with high-voltage $LiNi_{0.9}Co_{0.05}Mn_{0.05}O_2$ (NCM9) cathode and Li with 3D composite interlayer anode exhibit outstanding average coulombic efficiency (CE = 99.8%), excellent long-term cycling stability (>100 cycles at 0.3 C), and high capacity retention (>91% after 100 cycles) under ambient conditions. This work presents a scalable fabrication strategy that optimizes dynamic interfacial contact and suppresses Li void formation, offering a viable pathway for rationally designing composite anodes to achieve high-energy-density ASSLMBs.

## 2. Experimental

### 2.1. Materials

Graphitized multi-walled carbon nanotubes (GMWNTs, length > 50 nm) and fluorinated graphite (FG, thickness < 10 nm, flake size of ~10 μm) were purchased from Jiangsu XFNANO Materials Tech Co., Ltd. Polyvinylidene fluoride (PVDF; Alfa Aesar) and N-methyl-2-pyrrolidone (NMP; Aldrich) were employed as the binder and dispersant, respectively, for the interlayer slurry preparation. For the preparation of lithium metal anode, both lithium metal foil (thickness 50 μm; China Energy Lithium Co., Ltd.) and copper (Cu) foil were rolled together with a roller press, and then punched into a 9 mm diameter circular plate. The NCM9 cathode (67 wt% active material) was sourced from China First Automobile Group Co., Ltd., while the lithium phosphorus sulfur chloride (LPSC) electrolyte was obtained from Ganfeng Lithium Group Co., Ltd. All materials are kept in a glove box with water and oxygen values below 0.01 ppm.

### 2.2. Materials characterizations

The composite anode morphology was characterized by scanning electron microscopy (SEM, JSM 7401F at 5.0 kV), with simultaneous chemical composition analysis using energy-dispersive X-ray spectroscopy (EDS; Oxford Instruments). ASSBs were disassembled in an argon-filled glovebox ($H_2O$/$O_2$ < 0.1 ppm) and transferred to the characterization chamber via an argon-purged transfer vessel. Cross-sectional analysis of cycled cells was performed using a focused ion beam system (FIB, Crossbeam 340) at 20 nA beam current, enabling SEM examination of interfacial contact evolution during cycling. Phase composition before and after lithiation was determined by X-ray diffraction (XRD, Bruker D8 Advanced, Cu-$K_\alpha$ radiation, 40.0 kV, 120 mA). Surface chemistry evolution was investigated by X-ray photoelectron spectroscopy (XPS, Kratos Analytical, Axis Supra+, Al $K_\alpha$ radiation).

### 2.3. Preparation of composite anode

The slurry was prepared by mixing GMWNTs (Fig. S1), FG, and PVDF in NMP solution at a solid content of 6.9 wt%. The GMWNTs and FG were blended at varying weight ratios of 1:0, 10:1, and 5:5, respectively. Subsequently, the carbon composite and PVDF were homogenized at a 10:1 wt ratio, followed by the controlled addition of NMP solution to achieve optimal slurry viscosity. The slurry is then mixed by a ball mill at 1200 r $min^{-1}$ for 40 min. The interlayer was obtained by coating the slurry onto Cu foil by knife coater and dried in a vacuum oven at 120°C for over 12 h. The interlayer thickness was optimized based on the following criteria: complete Li surface coverage must be achieved, and thinner interlayers enable higher energy density. Experimental results demonstrated that a minimum thickness of 15 μm was required to ensure uniform coverage on Li, accounting for the intrinsic roughness of coated interlayers. The optimized interlayer thickness was determined to be 15 ± 0.5 μm. Finally, the interlayer and lithium metal were rolled together and left to stand at room temperature for 24 h, resulting in a composite anode with a lithiated interlayer, denoted as Li-$LNT_xF_y$ ($x$ = 10, 5 and $y$ = 1, 5).

### 2.4. Electrochemical performance

ASSBs were assembled in an argon-filled glovebox with $H_2O$ < 0.1 ppm and $O_2$ < 0.1 ppm. Critical current density (CCD) was evaluated using a stepwise current increment protocol: each charge/discharge cycle was conducted for 1 h, starting at 0.1 mA $cm^{-2}$ with 0.1 mA $cm^{-2}$ increments between steps. The full cells were cycled within the voltage range of 2.8–4.3 V at 0.3 C after one precycle at 0.05 C (1 C = 180 mA h $g^{-1}$). All mold cells were measured on a LAND multichannel battery testing system (Wuhan LAND Electronics Co., Ltd.) at 25°C. Electrochemical impedance spectroscopy (EIS) measurements were performed using an electrochemical workstation (Solartron EnergyLab XM). The EIS measurements featured an amplitude of 10 mV, spanning a frequency range from 1 MHz to 0.1 Hz. EIS was employed to non-destructively monitor interfacial evolution during cycling at a discharge current density of 0.5 mA $cm^{-2}$. Additionally, the distribution of relaxation times (DRT) analysis was performed using MATLAB GUI toolbox. All electrochemical measurements were conducted at room temperature (25°C).

## 3. Results and discussion

### 3.1. Preparation and characterization of 3D lithiated interlayer

The anode was fabricated by laminating the interlayer with Li foil, demonstrating scalable manufacturability (Fig. 1a). As shown in Fig. 1b, the intermediate layer exhibits apparent porosity before rolling, whereas it transforms into a dense intermediate layer after transferring (Fig. 1c). The $LNT_{10}F$ interlayer has a uniform thickness of approximately 15 μm, and its cross-sectional morphology was characterized by SEM. The $LNT_{10}F$ interlayer consists primarily of two elements, fluorine (F) and carbon (C), which are uniformly distributed throughout the layer as evidenced by EDS analysis, confirming the homogeneous mixing of GMWNTs and FG (Fig. 1d, e). When the Li stripping rate exceeds the Li replenishment rate, voids form at the Li/SSE interface during stripping, which increases cell overpotential and triggers both electrolyte reduction and Li dendrite growth. To mitigate these issues, we engineered a 3D porous interfacial layer on the Li surface. The graphitized carbon nanotubes construct an interconnected 3D porous architecture that enhances the interfacial contact area and lithium diffusion rate. The Gibbs free energy (Li + 6C → $LiC_6$, −10.59 kJ $mol^{-1}$) indicates that Li intercalation into carbon is thermodynamically spontaneous upon contact between metallic Li and GMWNTs. The interlayer components before and after lithiation were analyzed by XRD (Fig. 1f), revealing only characteristic peaks of $LiC_x$ ($x$ = 6, 12, 24) and Li. This indicates that lithiation occurred in the interlayer at room temperature, with GMWNTs reacting with lithium to form predominantly $LiC_6$ compounds. As shown in Fig. S2, the interlayer surface changed from black to golden in color. Furthermore, the composition of the interlayer before and after lithiation was analyzed by XPS. As shown in Fig. S4, the appearance of C–Li in the C 1*s* spectrum after lithiation further confirms the spontaneous reaction between Li and GMWNTs at room temperature, forming a highly ion-conductive $LiC_x$ phase. Additionally, the increased intensity of the Li–F peak in the F 1*s* spectrum (Fig. S5) confirms the formation of LiF through the reaction between FG and lithium at ambient temperature. The formed LiF can effectively suppress electrolyte reduction and maintain the stability of the anode/SSE interface.

### 3.2. Constructing Li diffusion pathways

To suppress the growth of Li voids by enhancing Li diffusion from the anode bulk to the interface, it is crucial to construct stable Li diffusion pathways. In the interlayer, the GMWNTs maintain a stable 3D skeleton structure at the interface. This ensures continuous contact between the anode and the SSE while providing channels for Li rapid diffusion.

The stability of Li diffusion pathways and the Li diffusion rate are correlated with the GMWNTs content in the interlayer. To evaluate the Li diffusion rates in anodes with varying GMWNTs contents, Li-$LNT_{10}F$ (GMWNTs:FG = 10:1) and Li-$LNT_5F_5$ (GMWNTs:FG = 1:1), anode||LiIn all-solid-state half-cells were assembled and operated at room temperature. The effective Li diffusion coefficient in the electrode is determined by the depletion time of Li at the anode/SSE interface. Assuming a classical chemical diffusion process driven by the Li concentration gradient in the alloy [61], the Sand equation can be applied [62]

$$\frac{1}{\sqrt{t_0}} = \frac{2}{c_0 F \sqrt{\pi D_{\text{eff}}}} I \tag{1}$$

Here, $c_0$ represents the initial Li concentration, and $t_0$ denotes the time at which the voltage in the discharge curve drops to −0.4 V, indicating Li depletion at the anode/SSE interface. Fig. 2a presents the plot of $t_0^{-1/2}$ versus $i$. The effective Li diffusion coefficient can be calculated from the slope of the fitted line, with the relevant data provided in Table S1. With increasing FG content, the effective diffusion coefficients for Li-$LNT_{10}F$ and Li-$LNT_5F_5$ were measured to be $9.62 \times 10^{-10}$, and $3.49 \times 10^{-10}$ $cm^2$ $s^{-1}$, respectively. In comparison, the Li metal anode exhibited a diffusion coefficient of $2.99 \times 10^{-10}$ $cm^2$ $s^{-1}$ (Fig. 2b). These results indicate that the GMWNTs content significantly affects the Li-ion diffusion kinetics at the anode. The system achieved optimal ion diffusion rates when the mass ratio of GMWNTs to FG reached 10:1 (Fig. 2c).

The Li-$LNT_xF_y$ anode also influences interfacial physical contact, thereby providing Li diffusion pathways. The interfacial physical contact was quantified based on interfacial impedance. Critical delithiation tests and EIS were conducted to investigate the evolution of interfacial physical contact in the Li-$LNT_xF_y$ anode. Fig. 2d demonstrates that the Li-$LNT_{10}F$ composite anode achieves a critical delithiation capacity of 12.96 mA h $cm^{-2}$, which is significantly higher than that of the Li metal anode (6.60 mA h $cm^{-2}$) under a stack pressure of 5 MPa. The stripping capability of the Li metal anode comprises two components: the Li diffusion flux and the creep flux. Since the FG component enhances the $Li^+$ diffusion coefficient while the lithiophilic GMWNTs provide abundant storage sites and transport pathways for Li ions, the Li-$LNT_xF_y$ anode consequently exhibits a higher Li diffusion coefficient. This improved transport property directly contributes to its superior critical delithiation capacity compared to conventional Li metal anodes.

Figs. S6 and S7 present the Nyquist plots illustrating the evolution of interfacial impedance during Li stripping in half-cells assembled with Li and Li-$LNT_xF_y$ anodes. The ohmic resistance, which reflects the intrinsic electrolyte impedance, is determined by the high-frequency intercept on the real axis. The evolution of ohmic impedance is attributed to variations in effective contact area within the cells. In Li||LiIn half-cells, the ohmic impedance initially decreases before increasing, whereas the Li-$LNT_{10}F$||LiIn system maintains essentially stable impedance. This contrast indicates that the pure Li anode undergoes significant contact changes with increasing delithiation capacity, while the Li-$LNT_xF_y$ anodes have nearly constant ohmic resistance throughout the entire delithiation process. The stability of the anode/SSE interface can be attributed to the formation of electrochemically stable LiF through the reaction between FG and lithium, which effectively suppresses interfacial side reactions and consequently reduces the $Li^+$ charge transfer resistance. Furthermore, the three-dimensional structure of GMWNTs helps maintain interfacial stability between the anode and SSE by preventing physical contact degradation that would otherwise obstruct $Li^+$ diffusion pathways.

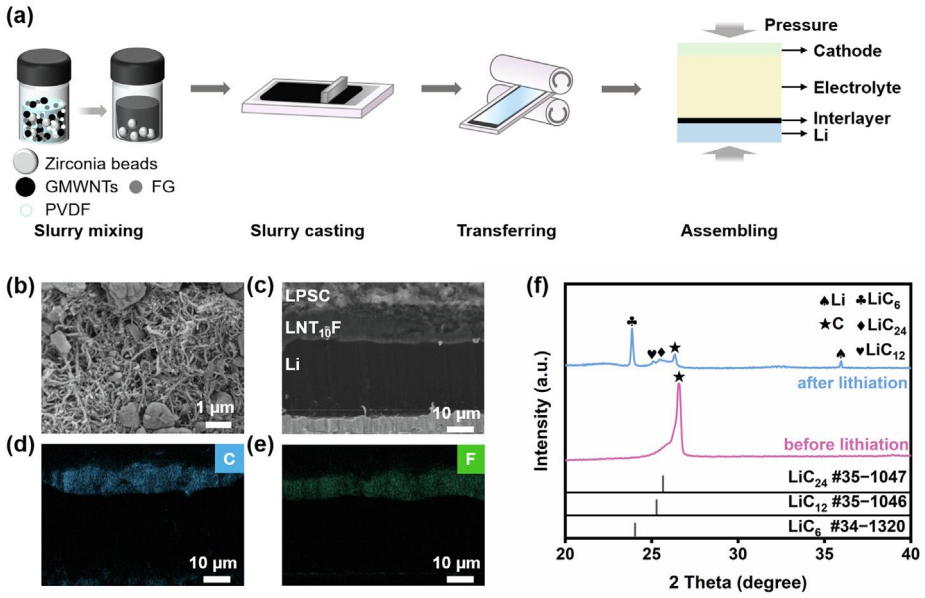


**Fig. 1.** Preparation and characterization of Li with $LNT_{10}F$ composite anodes. (a) Manufacturing steps include slurry mixing, casting, transferring, and final assembling; (b) morphology of the interlayer before transferring; (c) cross-sectional and local magnification of $LNT_{10}F$ SEM images; EDS images of (d) C and (e) F; (f) XRD analysis of $LNT_{10}F$ interlayer components before and after lithiation.

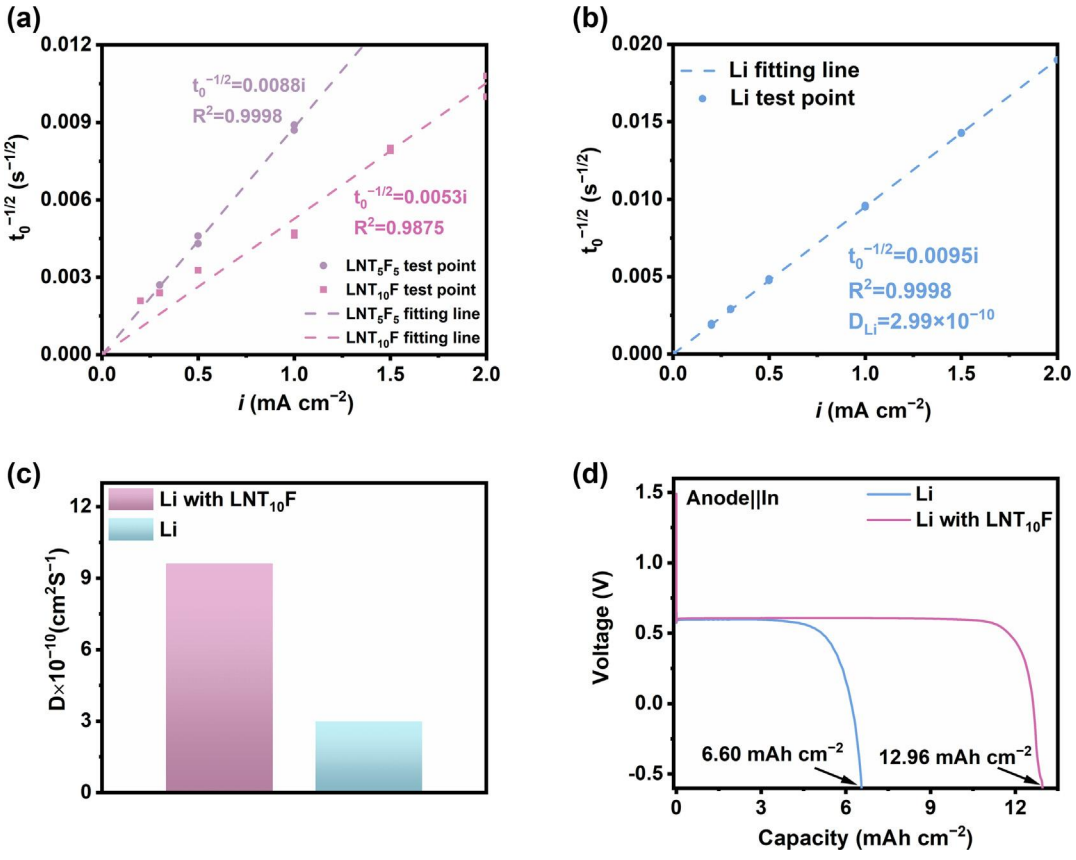


**Fig. 2.** Li diffusion rate evaluations of the different interlayers. Based on Sand's equation for estimating Li diffusion coefficients, the relationship between delithiation current density and depletion time ($t_0^{-1/2}$ vs. $i$) is presented: (a) interlayers with varied FG content, and (b) Li anode; (c) comparison of lithium diffusion coefficients; (d) voltage profiles of the Li with $LNT_{10}F$ composite anode and Li anode during delithiation at 0.5 mA $cm^{-2}$ under a stack pressure of 5 MPa at room temperature.

### 3.3. The evolution of interface contact

The interfacial morphology characterization further confirms the effectiveness of the Li-diffusion control strategy in suppressing Li void formation. Fig. 3a presents the morphological evolution of both Li and Li-$LNT_{10}F$ surfaces at varying delithiation capacities under a current density of 0.5 mA $cm^{-2}$. Initially, the Li metal anode exhibited a smooth surface morphology. However, due to

the limited $Li^+$ diffusion kinetics in the Li metal anode, shallow stripping voids emerged on the surface after 3.0 mA h $cm^{-2}$ delithiation. When the delithiation capacity increased to 6.0 mA h $cm^{-2}$, these voids grew significantly and eventually interconnected, forming an irregular porous structure. In contrast, under identical conditions, the Li-$LNT_{10}F$ surface maintained remarkable morphological stability, showing no significant changes even after 6.0 mA h $cm^{-2}$ delithiation, with only minimal micro-scale pitting observable. This superior stability originates from the effective suppression of Li void growth at the Li/SSE interface, which in conventional Li metal anodes results from vacancy accumulation during the delithiation process. In striking contrast, the Li-$LNT_{10}F$/SSE interface maintained intimate contact throughout the entire delithiation process (Fig. 4b). The GMWNTs establish a robust conductive network featuring abundant Li storage sites and efficient ion transport channels, which effectively mitigates the volumetric fluctuations of Li during cycling and thereby preserves the structural integrity of the host material. The LiF preformed by the reaction between FG and lithium effectively suppresses interfacial side reactions and maintains chemical stability at the interface. The synergistic effect between GMWNTs and FG enables dynamic interfacial stabilization and rapid Li-ion diffusion at the interface. Moreover, the critical delithiation capacity of the anode serves as a key indicator of its efficacy in suppressing Li void formation. Therefore, we systematically evaluated the critical delithiation capacity of Li-$LNT_{10}F$ at current densities of 2.0 and 3.0 mA $cm^{-2}$ (Fig. S8), with comparative analysis against previously reported systems. As demonstrated in Fig. S9, Li-$LNT_{10}F$ exhibits superior delithiation capability across various current densities, highlighting its exceptional advantage in suppressing interfacial void formation.

The evolution of ohmic impedance in half-cells reflects the increasing $R_{SSE}$ caused by contact loss at the anode interface (Fig. 3b). The quantitative relationship between contact area ($S$), contact retention ratio ($a$), and ohmic resistance ($R$) is mathematically described by Eqs. (2) and (3) [63].

$$a = \frac{S_{active}}{S_{initial}} \times 100\ \% \tag{2}$$

$$\frac{S_{active}}{S_{initial}} = \left(\frac{R_{SSE}}{R'_{SSE}}\right)^2 \tag{3}$$

Here, $S_{active}$ and $R'_{SSE}$ are the contact area and ohmic impedance after Li peeling, respectively. The ohmic impedance of the Li||LiIn half-cell increased significantly from an initial value of 8.5 to 31.2 Ω after Li stripping at 6.0 mA h $cm^{-2}$. The Li-$LNT_{10}F$||LiIn half-cell demonstrated stable ohmic impedance maintained at approximately 15.2 Ω (Fig. 3d). Notably, the Li-$LNT_{10}F$/SSE interface exhibited an impressive contact retention ratio of 95.3%, in stark contrast to the mere 7.4% observed at the Li/SSE interface, highlighting its exceptional interfacial stability (Fig. 3c). Therefore, the Li-diffusion regulation strategy effectively suppresses Li void formation at the anode interface and stabilizes dynamic interfacial contact.

### 3.4. Cyclic stability

To investigate the cycling stability of the Li-$LNT_{10}F$ anode, Li-$LNT_{10}F$||LPSC||NCM9 and Li||LPSC||NCM9 cells were fabricated for EIS measurements before and after 50 cycles. As shown in Fig. 4a, the polarization resistance of Li-$LNT_{10}F$||LPSC||NCM9 exhibits a slight increase after 50 cycles, whereas that of Li||LPSC||NCM9 shows a significant rise, indicating superior interfacial stability of the Li-$LNT_{10}F$/SSE interface. The results demonstrate that the application of a composite carbon layer can optimize battery interfacial contact. In the 3D $LNT_{10}F$ interlayer, the synergistic effect between fluorinated graphite and CNTs enables rapid lithium-ion conduction. Meanwhile, the conductive network of carbon nanotubes ensures efficient electron transfer. The interconnected three-dimensional architecture physically confines lithium deposition and accommodates volume changes during cycling. Cross-sectional SEM morphological characterization of the Li/SSE and Li-$LNT_{10}F$/SSE interfaces was conducted before and after cycling (Fig. 4b), providing direct visual evidence for the superior stability of dynamic contact at the Li-$LNT_{10}F$/SSE interface. The Li/SSE interface exhibited minor voids prior to Li stripping, followed by severe interfacial degradation and void enlargement after stripping. In contrast, the Li-$LNT_{10}F$/SSE interface maintained tight contact both before and after Li stripping.

### 3.5. Electrochemical performance of Li-$LNT_{10}F$ in ASSLMBs

To demonstrate the practical application potential of the interlayer, comprehensive electrochemical performance tests were conducted using both symmetric and full cell configurations. As shown in Fig. 5a, the Li symmetric cell experienced short-circuiting at a relatively low critical current density (CCD) of 0.8 mA $cm^{-2}$. This failure mechanism originated from contact loss due to Li void formation, which led to non-uniform $Li^+$ flux distribution and subsequent Li dendrite growth, ultimately causing battery failure. In contrast, the Li-$LNT_{10}F$ symmetric cell achieved a significantly higher CCD of 1.5 mA $cm^{-2}$ (Fig. 5b), attributable to both stable physical contact at the Li-$LNT_{10}F$/SSE interface and enhanced Li diffusion kinetics. The GMWNTs establish a stable porous mixed ionic-electronic conducting framework that mitigates interfacial contact degradation caused by Li void formation. The LiF layer promotes homogeneous Li deposition, thereby reducing localized $Li^+$ flux and effectively increasing the CCD. Furthermore, the LiF interphase promotes more uniform charge density distribution while suppressing excess electron accumulation at the interface. This interphase facilitates uniform Li ion transport across the interface and enables homogeneous Li deposition, thereby effectively suppressing Li dendrite growth. During the deposition process, the $Li^0$ generated on the surface diffuses into the $LNT_{10}F$ interlayer, promoting uniform deposition of metallic Li.

Furthermore, to evaluate the impact of stabilized anode/SSE interfacial contact on practical battery performance, full cells were constructed with NCM9 cathodes and tested at room temperature. Fig. 5c presents the galvanostatic charge/discharge curves of the cells cycled at various C-rates from 0.1 to 0.5 C. The cells with Li-$LNT_{10}F$ anode demonstrated higher discharge capacities across all current densities. When the current density returned to 0.1 C, the specific discharge capacity reached 167.5 mA h $g^{-1}$, demonstrating excellent rate capability and cycling stability. The Li-$LNT_{10}F$||LPSC||NCM9 cell delivered higher specific discharge capacities (Fig. 5e) of 168.9, 147.5, 130.1, 119.6, and 109.2 mA h $g^{-1}$ at 0.1, 0.2, 0.3, 0.4, and 0.5 C, respectively, compared to the Li||LPSC||NCM9 cell under the same current densities (Fig. 5d). Fig. 5f shows the charge-discharge curves of the Li||LPSC||NCM9 at different cycle numbers, with an initial discharge capacity of 156.3 mA h $g^{-1}$, and a voltage drop was observed during charging due to short circuit. Fig. 5g shows the charge-discharge curves of the Li-$LNT_{10}F$||LPSC||NCM9 at different cycle numbers, with an initial discharge capacity of 148.1 mA h $g^{-1}$. Fig. 5h presents the galvanostatic cycling performance of full cells with Li-$LNT_{10}F$ and Li anodes at room temperature. The Li||LPSC||NCM9 cell exhibited fluctuating Coulombic efficiency after 46 cycles, indicating battery failure. In contrast, the cell employing the Li-$LNT_{10}F$ anode maintained stable cycling over 100 cycles at a current density of 0.3 C. This improvement can be attributed to the stable interfacial contact between Li-$LNT_{10}F$ and the SSE during cycling. Such interfacial

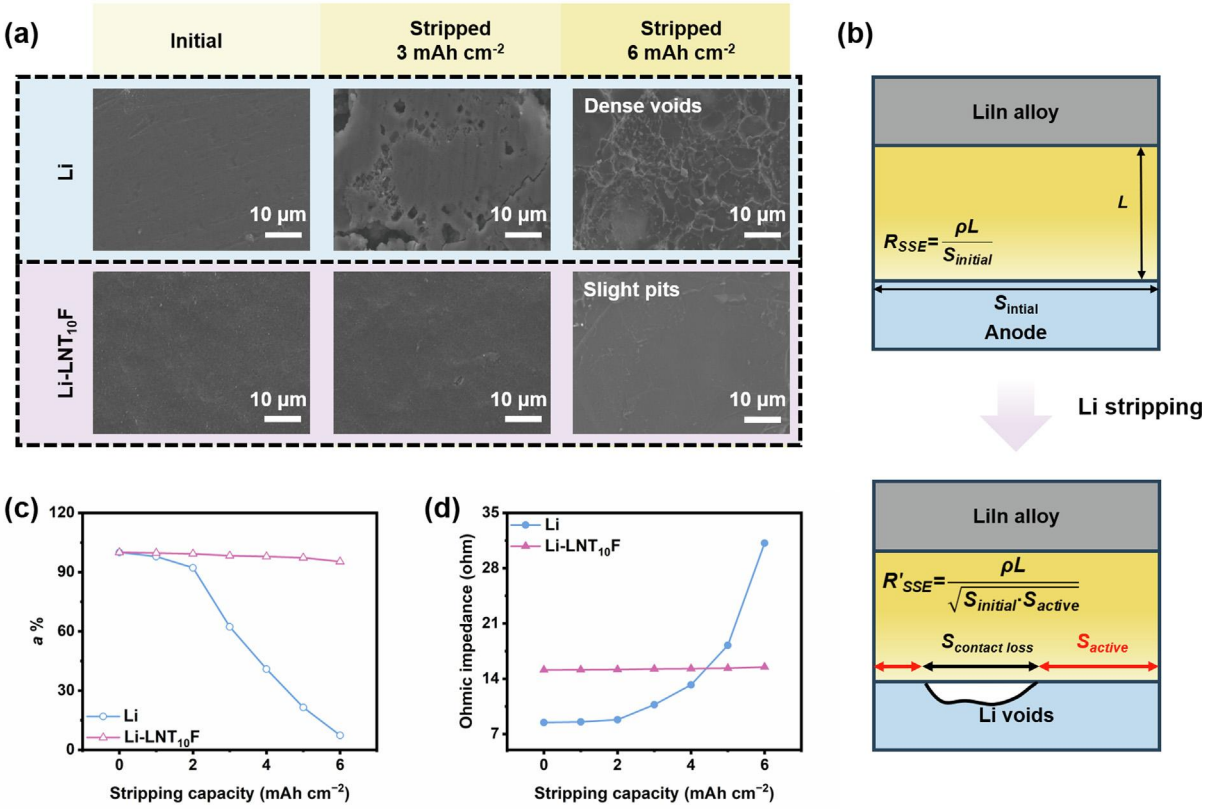


**Fig. 3.** Interface contact evolution of Li and Li with $LNT_{10}F$. (a) SEM image of surface morphological evolution during continuous Li stripping of conventional Li metal anode and Li-$LNT_{10}F$ composite anode at 0.5 mA $cm^{-2}$; (b) The schematic shows the $R_{SSE}$ increase due to interface contact loss; (c) Contact retention ratio a of Li/SSE and Li-x$LNT_{10}F$/SSE interface during Li stripping; (d) The evolution of the Ohmic impedance of Li||LiIn and Li-$LNT_{10}F$||LiIn half-cell during Li stripping.

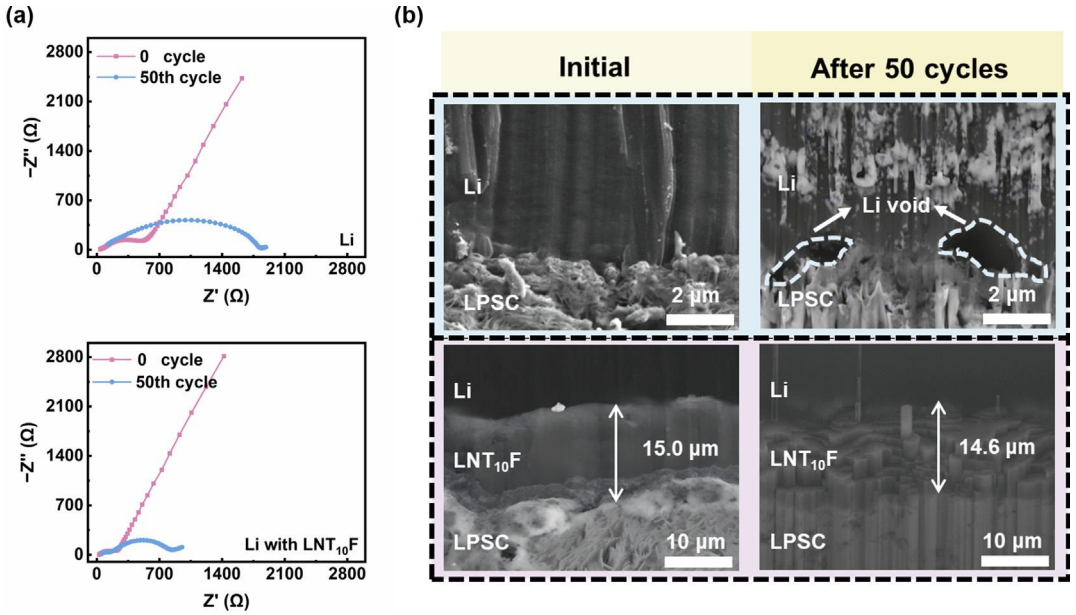


**Fig. 4.** Characterization of anode/SSE interfaces before cycling and after 50 cycles: (a) Nyquist plots of full cells with Li metal anodes and composite Li metal anodes with $LNT_{10}F$; (b) Cross-sectional SEM images of Li/SSE and Li$GM_{10}F$/SSE interfaces.

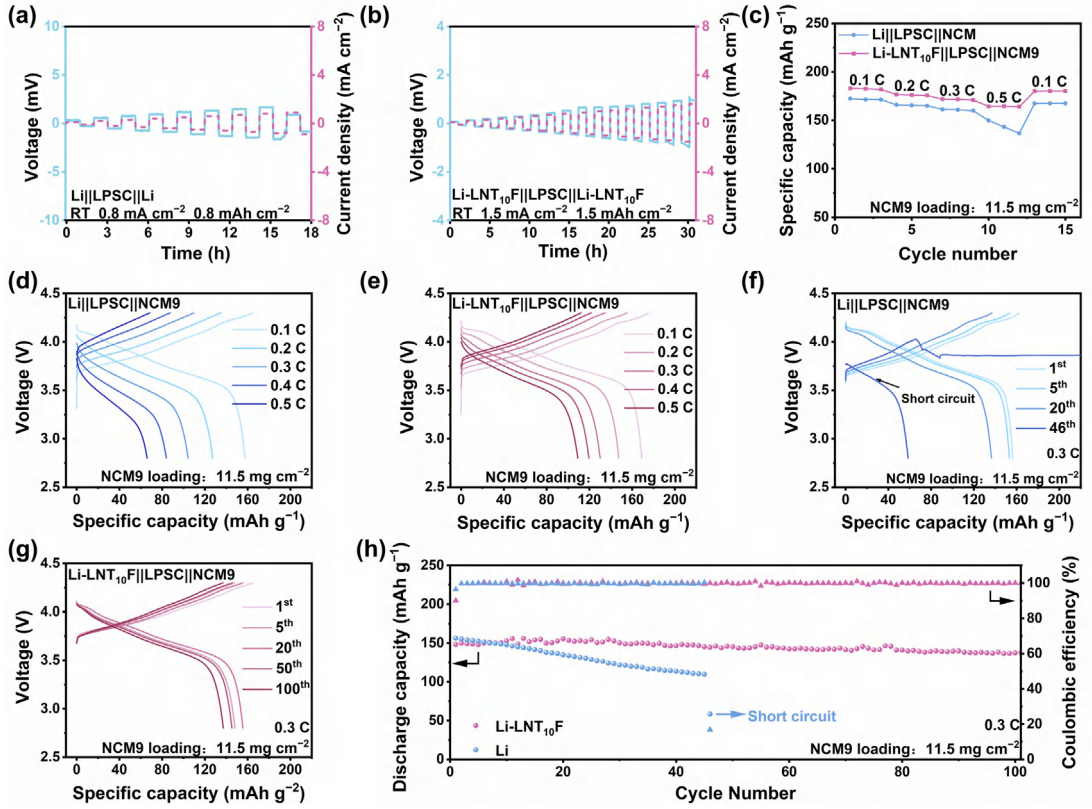


**Fig. 5.** Electrochemical properties of ASSLMBs. (a, b) Critical current density of symmetrical cells with Li and Li-LNT$_{10}$F anodes; (c) Rate performances of full cells (1 C = 180 mA h g$^{-1}$); (d, e) Charge-discharge curves of Li||LPSC||NCM9 and Li-LNT$_{10}$F||LPSC||NCM9 cells at different current densities, respectively; (f, g) Charge-discharge curves of Li||LPSC||NCM9 and Li-LNT$_{10}$F||LPSC||NCM9 at different cycle numbers, respectively; (h) Long-term cycling stability of full cells at 0.3 C.

stability facilitates uniform Li deposition, suppresses interfacial degradation, and consequently enhances cycling performance.

## 4. Conclusions

Regulation of Li diffusion is critical for preventing void formation at the anode/SSE interface. The GMWNTs in the 3D interlayer establish stable interfacial contact with the SSE, enhancing $Li^+$ transport kinetics and serving as reliable Li diffusion pathways. The formed LiF through FG-lithium interaction not only mitigates side reactions but also preserves interfacial chemical stability. The synergistic interaction between GMWNTs and FG in the interlayer significantly enhances Li diffusion kinetics, achieving an elevated diffusion coefficient of $9.62 \times 10^{-10}$ cm$^2$ s$^{-1}$. The Li-LNT$_{10}$F/SSE interface maintains structural integrity even after a high areal capacity of 12.96 mA h cm$^{-2}$. The full cell incorporating an NCM9 cathode demonstrates outstanding cycling stability, retaining over 91 % capacity after 100 cycles at room temperature. This work proposes an effective interface engineering strategy for high-safety ASSLMBs with high energy densities.

## CRediT authorship contribution statement

**Zi-Ning Cheng:** Writing – original draft, Methodology, Investigation, Formal analysis, Conceptualization. **Xue-Yan Huang:** Writing – review & editing, Investigation, Funding acquisition, Formal analysis, Conceptualization. **Chen-Zi Zhao:** Writing – review & editing, Supervision, Investigation, Funding acquisition, Conceptualization. **Fang Fu:** Investigation. **Jun-Dong Zhang:** Investigation. **Jiang-Kui Hu:** Investigation. **Yuqiong Mao:** Investigation. **Lan-guang Lu:** Investigation. **Chun-Li Guo:** Supervision, Funding acquisition. **Qiang Zhang:** Writing – review & editing, Supervision.

## Declaration of competing interest

The authors declare that they have no known competing financial interests or personal relationships that could have appeared to influence the work reported in this paper.

## Acknowledgments

We thank the Shanxi Province Science Foundation (20210302123150), the National Key Research and Development Program (2021YFB2500300), the National Natural Science Foundation of China (223B1012, 22409114), the Beijing Natural Science Foundation (L243019), the Anhui Science and Technology Innovation Tackling Key Problems Plan Project (202423h08050005), and the China Postdoctoral Science Foundation (2023M731920).

## Appendix A. Supplementary material

Supplementary data to this article can be found online at https://doi.org/10.1016/j.jechem.2025.07.033.

## References

[1] S. Xin, X. Zhang, L. Wang, H.J. Yu, X. Chang, Y.M. Zhao, Q.H. Meng, P. Xu, C.Z. Zhao, J.H. Chen, H.C. Lu, X.R. Kong, J.L. Wang, K. Chen, G. Huang, X.B. Zhang, Y. Su, Y. Xiao, S.L. Chou, S.L. Zhang, Z.P. Guo, A.B. Du, G.L. Cui, G.J. Yang, Q. Zhao, L. B. Dong, D. Zhou, F.Y. Kang, H. Hong, C.Y. Zhi, Z.Z. Yuan, X.F. Li, Y.F. Mo, Y.Z. Zhu, D.F. Yu, X.C. Lei, J.X. Zhao, J.Y. Wang, D. Su, Y.G. Guo, Q. Zhang, J. Chen, L.J. Wan, Sci. Chin. Chem. 67 (2024) 13–42.

[2] J.G. Liu, B.H. Li, J.H. Cao, X. Xing, G. Cui, J. Energy Chem. 91 (2024) 73–98.
[3] T.Q. Yang, C. Wang, W.K. Zhang, Y. Xia, H. Huang, Y.P. Gan, X.P. He, X.H. Xia, X.Y. Tao, J. Zhang, J. Energy Chem. 84 (2023) 189–209.
[4] L. Zheng, R. Lv, C. Luo, Y. Guo, M. Yang, K. Hu, K. Wang, L. Li, F. Wu, R. Chen, Adv. Energy Mater. 14 (2024) 2402042.
[5] L.K. Chen, P.R. Shi, T. Gu, J.S. Mi, K. Yang, L. Zhao, J.S. Lv, M. Liu, Y.B. He, F.Y. Kang, eScience 5 (2025) 100277.
[6] Y. Guo, S.C. Wu, Y.B. He, F.Y. Kang, L.Q. Chen, H. Li, Q.H. Yang, eScience 2 (2022) 138–163.
[7] Y.G. Lee, S. Fujiki, C. Jung, N. Suzuki, N. Yashiro, R. Omoda, D.S. Ko, T. Shiratsuchi, T. Sugimoto, S. Ryu, J.H. Ku, T. Watanabe, Y. Park, Y. Aihara, D. Im, I. T. Han, Nat. Energy 5 (2020) 299–308.
[8] Z. Shen, X. Jin, J. Tian, M. Li, Y. Yuan, S. Zhang, S. Fang, X. Fan, W. Xu, H. Lu, J. Lu, H. Zhang, Nat. Catal. 5 (2022) 555–563.
[9] P. Shi, L.P. Hou, C.B. Jin, Y. Xiao, Y.X. Yao, J. Xie, B.Q. Li, X.Q. Zhang, Q. Zhang, J. Am. Chem. Soc. 144 (2022) 212–218.
[10] Y.C. Gao, N. Yao, X. Chen, L.G. Yu, R. Zhang, Q. Zhang, J. Am. Chem. Soc. 145 (2023) 23764–23770.
[11] H. Wan, Z. Wang, W. Zhang, X. He, C. Wang, Nature 623 (2023) 739–744.
[12] H. Wan, Z. Wang, S. Liu, B. Zhang, X. He, W. Zhang, C. Wang, Nat. Energy 8 (2023) 473–481.
[13] D.H.S. Tan, Y.T. Chen, H. Yang, W. Bao, B. Sreenarayanan, J.M. Doux, W. Li, B. Lu, S.Y. Ham, B. Sayahpour, J. Scharf, E.A. Wu, G. Deysher, H.E. Han, H.J. Hah, H. Jeong, J.B. Lee, Z. Chen, Y.S. Meng, Science 373 (2021) 1494–1499.
[14] L.S. Li, Y.F. Deng, G.H. Chen, J. Energy Chem. 50 (2020) 154–177.
[15] H. Su, J. Li, Y. Zhong, Y. Liu, X. Gao, J. Kuang, M. Wang, C. Lin, X. Wang, J. Tu, Nat. Commun. 15 (2024) 4202–4211.
[16] D. Spencer-Jolly, V. Agarwal, C. Doerrer, B. Hu, S. Zhang, D.L.R. Melvin, H. Gao, X. Gao, P. Adamson, O.V. Magdysyuk, P.S. Grant, R.A. House, P.G. Bruce, Joule 7 (2023) 503–514.
[17] P. Shi, J. Ma, M. Liu, S. Guo, Y. Huang, S. Wang, L. Zhang, L. Chen, K. Yang, X. Liu, Y. Li, X. An, D. Zhang, X. Cheng, Q. Li, W. Lv, G. Zhong, Y.B. He, F. Kang, Nat. Nanotechnol. 18 (2023) 602–610.
[18] B. Shao, Y. Huang, F. Han, Adv. Energy Mater. 13 (2023) 2204098.
[19] H. Pan, M. Zhang, Z. Cheng, H. Jiang, J. Yang, P. Wang, P. He, H. Zhou, Sci. Adv. 8 (2022) 4372–4379.
[20] H. Pan, L. Wang, Y. Shi, C. Sheng, S. Yang, P. He, H. Zhou, Nat. Commun. 15 (2024) 2263–2274.
[21] J. Kasemchainan, S. Zekoll, D. Spencer-Jolly, Z. Ning, G.O. Hartley, J. Marrow, P. G. Bruce, Nat. Mater. 18 (2019) 1105–1111.
[22] Z. Ning, D.S. Jolly, G. Li, R. De Meyere, S.D. Pu, Y. Chen, J. Kasemchainan, J. Ihli, C. Gong, B. Liu, D.L.R. Melvin, A. Bonnin, O. Magdysyuk, P. Adamson, G.O. Hartley, C.W. Monroe, T.J. Marrow, P.G. Bruce, Nat. Mater. 20 (2021) 1121–1129.
[23] C. Rosenbach, F. Walther, J. Ruhl, M. Hartmann, T.A. Hendriks, S. Ohno, J. Janek, W.G. Zeier, Adv. Energy Mater. 13 (2023) 2203673.
[24] X. Hu, Z. Zhang, X. Zhang, Y. Wang, X. Yang, X. Wang, M. Fayena-Greenstein, H. A. Yehezkel, S. Langford, D. Zhou, B. Li, G. Wang, D. Aurbach, Nat. Rev. Mater. 9 (2024) 305–320.
[25] V. Faka, M.T. Agne, M.A. Lange, D. Daisenberger, B. Wankmiller, S. Schwarzmüller, H. Huppertz, O. Maus, B. Helm, T. Böger, J. Hartel, J.M. Gerdes, J.J. Molaison, G. Kieslich, M.R. Hansen, W.G. Zeier, J. Am. Chem. Soc. 146 (2024) 1710–1721.
[26] S.Y. Ham, H. Yang, O. Nunez-Cuacuas, D.H.S. Tan, Y.T. Chen, G. Deysher, A. Cronk, P. Ridley, J.M. Doux, E.A. Wu, J. Jang, Y.S. Meng, Energy Storage Mater. 55 (2022) 455–462.
[27] J. Gu, Z. Liang, J. Shi, Y. Yang, Adv. Energy Mater. 13 (2022) 2203153.
[28] W. Huang, Y. Ye, H. Chen, R.A. Vilá, A. Xiang, H. Wang, F. Liu, Z. Yu, J. Xu, Z. Zhang, R. Xu, Y. Wu, L.Y. Chou, H. Wang, J. Xu, D.T. Boyle, Y. Li, Y. Cui, Nat. Commun. 13 (2022) 7091–7099.
[29] H.H. Chen, X. Cao, M.J. Huang, X.Z. Ren, Y.B. Zhao, L. Yu, Y. Liu, L.B. Zhong, Y.J. Qi, J. Energy Chem. 88 (2024) 282–292.
[30] S. Wenzel, T. Leichtweiss, D. Kruger, J. Sann, J. Janek, Solid State Ion. 278 (2015) 98–105.
[31] D. Rehnlund, Z.H. Wang, L. Nyholm, Adv. Mater. 34 (2022) 2108827.
[32] J. Haruyama, K. Sodeyama, Y. Tateyama, ACS Appl. Mater. Inter. 9 (2017) 286–292.
[33] Y. Wang, T. Liu, J. Kumar, ACS Appl. Mater. Inter. 12 (2020) 34771–34776.
[34] J. Kasemchainan, S. Zekoll, D.S. Jolly, Z. Ning, G.O. Hartley, J. Marrow, P.G. Bruce, Nat. Mater. 18 (2019) 1105–1111.
[35] M.J. Wang, R. Choudhury, J. Sakamoto, Joule 3 (2019) 2165–2178.
[36] K. Lu, C.F. Huo, Y. He, J. Yin, J. Liu, Q. Peng, W.P. Guo, Y. Yang, Y.W. Li, X.D. Wen, J. Phys. Chem. C 122 (2018) 23191–23199.
[37] F. Zhang, A.M. Walker, K. Wright, J.D. Gale, J. Mater. Chem. 20 (2010) 10445–10451.
[38] H.H. Yan, K. Tantratian, K. Ellwood, E.T. Harrison, M. Nichols, X.Y. Cui, L. Chen, Adv. Energy Mater. 12 (2022) 2102283.
[39] S. Lee, K.-S. Lee, S. Kim, K. Yoon, S. Han, M.H. Lee, Y. Ko, J.H. Noh, W. Kim, K. Kang, Sci. Adv. 8 (2022) eabq0153.
[40] K.K. Fu, Y. Gong, Z. Fu, H. Xie, Y. Yao, B. Liu, M. Carter, E. Wachsman, L. Hu, Angew. Chem. Int. Ed. Engl. 56 (2017) 14942–14947.
[41] X.G. Han, Y.H. Gong, K. Fu, X.F. He, G.T. Hitz, J.Q. Dai, A. Pearse, B.Y. Liu, H. Wang, G. Rubloff, Y.F. Mo, V. Thangadurai, E.D. Wachsman, L.B. Hu, Nat. Mater. 16 (2017) 572–579.
[42] W. Luo, Y.H. Gong, Y.Z. Zhu, K.K. Fu, J.Q. Dai, S.D. Lacey, C.W. Wang, B.Y. Liu, X. G. Han, Y.F. Mo, E.D. Wachsman, L.B. Hu, J. Am. Chem. Soc. 138 (2016) 12258–12262.
[43] C.L. Tsai, V. Roddatis, C.V. Chandran, Q. Ma, S. Uhlenbruck, M. Bram, P. Heitjans, O. Guillon, ACS Appl. Mater. Inter. 8 (2016) 10617–10626.
[44] Y. Shao, H. Wang, Z. Gong, D. Wang, B. Zheng, J. Zhu, Y. Lu, Y.S. Hu, X. Guo, H. Li, X. Huang, Y. Yang, C.W. Nan, L. Chen, ACS Energy Lett. 3 (2018) 1212–1218.
[45] H. Huo, J. Gao, N. Zhao, D. Zhang, N.G. Holmes, X. Li, Y. Sun, J. Fu, R. Li, X. Guo, X. Sun, Nat. Commun. 12 (2021) 176.
[46] J. Duan, W. Wu, A.M. Nolan, T. Wang, J. Wen, C. Hu, Y. Mo, W. Luo, Y. Huang, Adv. Mater. 31 (2019) 1807243.
[47] M. Du, K. Liao, Q. Lu, Z. Shao, Energy Environ. Sci. 12 (2019) 1780–1804.
[48] J. Kang, N. Deng, Y. Liu, Z. Yan, L. Gao, H. Xiang, L. Zhang, G. Wang, B. Cheng, W. Kang, Energy Storage Mater. 52 (2022) 130–160.
[49] H. Gao, X. Ai, H. Wang, W. Li, P. Wei, Y. Cheng, S. Gui, H. Yang, Y. Yang, M.S. Wang, Nat. Commun. 13 (2022) 5050.
[50] J.H. Han, R. Cheng, L.Q. Liu, H. Ohno, S. Fukami, Nat. Mater. 22 (2023) 684–695.
[51] G. Kim, J.W. Lee, K.Y. Zhao, T. Kim, W. Kim, J.W. Oh, K. Lee, J. Jang, G.T. Zan, J.W. Park, S. Lee, S.Y. Kim, W. Jiang, S.Y. Li, C. Park, Energy Environ. Sci. 17 (2024) 134–148.
[52] W.J. Jeong, C. Wang, S.G. Yoon, Y. Liu, T. Chen, M.T. McDowell, ACS Energy Lett. 9 (2024) 2554–2563.
[53] J.S. Kim, G. Yoon, S. Kim, S. Sugata, N. Yashiro, S. Suzuki, M.J. Lee, R. Kim, M. Badding, Z. Song, J. Chang, D. Im, Nat. Commun. 14 (2023) 782.
[54] M. Yang, Y. Wu, K. Yang, Z. Wang, T. Ma, D. Wu, F. Xu, L. Yang, P. Lu, J. Peng, Q. Gao, X. Zhu, Z. Jiang, L. Chen, H. Li, F. Wu, Adv. Energy Mater. 14 (2024) 2303229.
[55] S.J. Jeon, C. Hwang, H.S. Kim, J. Park, J.Y. Hwang, Y. Jung, R. Choi, M.S. Song, Y.J. Lee, J.S. Yu, Y.C. Jung, Adv. Energy Mater. 14 (2024) 2402887.
[56] Z. Wang, Z. Mu, T. Ma, W. Yan, D. Wu, Y. Li, M. Yang, J. Peng, Y. Xia, S. Shi, L. Chen, H. Li, F. Wu, Adv. Energy Mater. 14 (2024) 2400003.
[57] T. Krauskopf, F.H. Richter, W.G. Zeier, J. Janek, Chem. Rev. 120 (2020) 7745–7794.
[58] Y. Lu, C.Z. Zhao, J.K. Hu, S. Sun, H. Yuan, Z.H. Fu, X. Chen, J.Q. Huang, M. Ouyang, Q. Zhang, Sci. Adv. 8 (2022) add0510.
[59] T. Shi, Y.Q. Zhang, Q. Tu, Y. Wang, M.C. Scott, G. Ceder, J. Mater. Chem. A 8 (2020) 17399–17404.
[60] H. Yan, K. Tantratian, K. Ellwood, E.T. Harrison, M. Nichols, X. Cui, L. Chen, Adv. Energy Mater. 12 (2021) 2102283.
[61] Y. Chen, Z. Wang, X. Li, X. Yao, C. Wang, Y. Li, W. Xue, D. Yu, S.Y. Kim, F. Yang, A. Kushima, G. Zhang, H. Huang, N. Wu, Y.W. Mai, J.B. Goodenough, J. Li, Nature 578 (2020) 251–255.
[62] M. Wang, J.B. Wolfenstine, J. Sakamoto, Electrochim. Acta 296 (2019) 842.
[63] F. Yonemoto, A. Nishimura, M. Motoyama, N. Tsuchimine, S. Kobayashi, Y. Iriyama, J. Pow. Sourc. 343 (2017) 207–215.
[64] Y. Qi, C. Ban, S.J. Harris, Joule 4 (2020) 2599–2608.
[65] J.M. Doux, H. Nguyen, D.H.S. Tan, A. Banerjee, X. Wang, E.A. Wu, C. Jo, H. Yang, Y.S. Meng, Adv. Energy Mater. 10 (2019) 1903253.
[66] T. Krauskopf, B. Mogwitz, H. Hartmann, D.K. Singh, W.G. Zeier, J. Janek, Adv. Energy Mater. 10 (2020) 2000945.
[67] T. Krauskopf, B. Mogwitz, C. Rosenbach, W.G. Zeier, J. Janek, Adv. Energy Mater. 9 (2019) 1902568.
[68] T. Fuchs, C.G. Haslam, A.C. Moy, C. Lerch, T. Krauskopf, J. Sakamoto, F.H. Richter, J. Janek, Adv. Energy Mater. 12 (2022) 2201125.
[69] S. Xu, D.W. McOwen, C. Wang, L. Zhang, W. Luo, C. Chen, Y. Li, Y. Gong, J. Dai, Y. Kuang, C. Yang, T.R. Hamann, E.D. Wachsman, L. Hu, Nano Lett. 18 (2018) 3926–3933.
[70] C. Wang, Y. Gong, B. Liu, K. Fu, Y. Yao, E. Hitz, Y. Li, J. Dai, S. Xu, W. Luo, E.D. Wachsman, L. Hu, Nano Lett. 17 (2017) 565–571.